Front. Earth Sci. 2021, 15(4): 790–802
https://doi.org/10.1007/s11707-021-0869-x

RESEARCH ARTICLE

Numerical modeling of the dynamic variation in multiphase CH_4 during CO_2 enhanced gas recovery from depleted shale reservoirs

Lijun CHENG[1], Ye ZHANG[1], Jun LIU (✉)[1,2], Zhaohui LU[1], Chunlin ZENG[1], Peng ZHAO (✉)[3]

1 Key Laboratory of Shale Gas Exploration (Ministry of Natural Resources), Chongqing Institute of Geology and Mineral Resources, Chongqing 401120, China
2 Institute of New Energy and Low-Carbon Technology, Sichuan University, Chengdu 610065, China
3 College of Architecture and Environment, Sichuan University, Chengdu 610065, China

Abstract Regarding CO_2 enhanced shale gas recovery, this work focuses on changes in the multiphase (free/adsorbed) CH_4 in the process of CO_2 enhanced shale gas recovery, by utilizing a rigorous numerical model with real geological parameters. This work studies nine injection well (IW) and CH_4 production well (PW) combinations of CO_2 to determine the influence of IW and PW locations on the dynamic interaction of multiphase CH_4 during 10000 d of CO_2 injection. The results indicate that the content of both the adsorbed CH_4 and free CH_4 is strongly variable before (and during) the CO_2-CH_4 displacement. In addition, during the simulation process, the proportion of the adsorbed CH_4 among all extracted CH_4 phases dynamically increases first and then tends to stabilize at 70%–80%. Moreover, the IW-PWs combinations significantly affect the outcomes of CO_2 enhanced shale gas recovery – for both the proportion of adsorbed/free CH_4 and the recovery efficiency. A longer IW-PW distance enables more adsorbed CH_4 to be recovered but results in a lower efficiency of shale gas recovery. Basically, a shorter IW-PWs distance helps recover CH_4 via CO_2 injection if the IW targets the bottom layer of the Wufeng-Longmaxi shale formation. This numerical work expands the knowledge of CO_2 enhanced gas recovery from depleted shale reservoirs.

Keywords CO_2-CH_4 displacement, free gas, Longmaxi shale, CH_4 desorption, numerical simulation

Received October 21, 2020; accepted January 4, 2021

E-mails: j.liu@scu.edu.cn (J. Liu)
scu_zhaopeng@163.com (P. Zhao)

1 Introduction

As a well-known clean energy source, so-called shale gas with CH_4 as the main component is lauded as having a significant supply to meet the increasing energy consumption worldwide (Hou et al., 2018; Cui et al., 2019; Li et al., 2019a; Li et al., 2019b; Gao et al., 2020), making the improvement in gas recovery from tight shale reservoirs a popular topic of study in the petroleum and natural gas exploration domains worldwide (Liu et al., 2016; Zhang et al., 2017; Li et al., 2018; Guo et al., 2020b; Li et al., 2020a; Mazumder et al., 2020). Against this background, the injection of CO_2 into shale reservoirs has received widespread public attention because it enables simultaneous CO_2 sequestration and enhanced gas recovery (CS-EGR) as a result of CO_2/CH_4 interactions in the shale (Chi et al., 2017; Fan et al., 2018; Zhou et al., 2019a; Klewiah et al., 2020; Li et al., 2020b). Therefore, the shale-based CS-EGR technique has been researched in numerous studies, which clarify that it is feasible in theory but difficult in practice because this technique includes strategy optimization, site characterization/monitoring, hazard assessment and management, etc. (Abidoye et al., 2015; Pan et al., 2018; Luo et al., 2019; Zhang et al., 2019; Chen et al., 2020; Iddphonce et al., 2020; Wang et al., 2020). In other words, CS-EGR in shale has been popularized, but full deployment worldwide requires more research to deepen the knowledge of this promising technique.

Basically, in the investigation of shale-based CS-EGR operation, the approaches adopted in the existing literature vary, but some sound achievements are as follows (Iddphonce et al., 2020; Klewiah et al., 2020; Li et al., 2020c). Experiments with low-field NMR scanning have

exhibited the desorption of adsorbed CH_4 and CO_2/CH_4 competitive adsorption behavior after CO_2 is injected into shale samples (Liu et al., 2017b; Liu et al., 2019). Another self-designed experiment has confirmed that the preferential adsorption ratio of CO_2 over CH_4 varies between 1.66 and 8.32 (Zhou et al., 2019c). In addition, numerical simulations have been used to accurately characterize the effectiveness of shale-based CS-EGR. For example, a numerical approach was used to show that the proportion of CO_2 in a CO_2-N_2 mixture significantly affects the improved recovery efficiency of shale gas (Li and Elsworth, 2019). For example, the results of grand canonical Monte Carlo simulations have indicated that a higher water content is helpful in trapping more CO_2 during the shale-based CS-EGR process (Zhou et al., 2019b). The majority of interest in CS-EGR in shale has focused on mainly the CH_4 in the adsorbed phase (Wang et al., 2018; Zhang et al., 2020; Liu et al., 2021a; Liu et al., 2021b), causing research on free CH_4 during the CS-EGR process to be lacking to some extent. However, free CH_4 inevitably emerges in the inner spaces (e.g., pores and fractures) of shale during CS-EGR (Fathi and Akkutlu, 2014). Therefore, compared with the considerable attention paid to adsorbed CH_4, the relatively insubstantial attention paid to free CH_4 tends to limit the awareness of the coordinated behavior of CH_4 in multiple phases (adsorbed/free) and thus the comprehensive understanding of shale-based CS-EGR.

Recently, in some investigations on CO_2-enhanced shale gas recovery, how free CH_4 interacts with adsorbed CH_4 in shale has been studied. For example, the proportion of free CH_4 to adsorbed CH_4 during shale-based CS-EGR was explored and the influence of free CH_4 on CO_2 sequestration in shale was investigated by performing numerical work (Tao et al., 2014; Mohagheghian et al., 2019). Nevertheless, existing numerical simulations relating to the interaction between free CH_4 and adsorbed CH_4 are mainly organized using a plain mathematical model with only a single layer or/and isotropic conditions considered, in the process of CO_2 enhanced shale gas recovery. This phenomenon does not conform with the fact that field shale reservoirs is always characterized as multilayer and heterogeneous (Su et al., 2007; Pan et al., 2015; Liu et al., 2017a). Under such circumstances, more attention should be paid to the dynamic interaction of free CH_4 and adsorbed CH_4 in shale after CO_2 is injected, helping promote the development of this CS-EGR technique, which is what this work focuses on.

This work develops an advanced thermal-hydraulic-mechanical (THM) coupled model, where the rock deformation, competitive binary gas sorption, gas and water two-phase flow and thermal expansion in the dual-porosity system are comprehensively considered, using the modeling software COMSOL Multiphysics. This novel model is used to reflect the vertical heterogeneity of the porosity, permeability, Poisson's ratio, Young's modulus and Langmuir volume/pressure (CH_4 and CO_2) of a depleted shale formation from the Upper Ordovician Wufeng formation to the lower Silurian Longmaxi formation (WL, for short), ensuring that the model matches the real reservoir conditions as accurately as possible, to focus on the scenarios of most interest. Herein, the WL shale is chosen as the representative example case because of its promising potential for shale gas exploration and exploitation in the Sichuan Basin (Liu et al., 2017a; Liu et al., 2017c; Shan et al., 2017). Accordingly, the dynamic variation in and the outputs of multiphase CH_4 (free/adsorbed) during the CS-EGR process are investigated under nine different arrangements of CO_2 injection well (IW) and CH_4 production well (PW). Furthermore, the implications of this work for CO_2-enhanced shale gas recovery are also suggested. Through these efforts, this work offers a new modeling concept and a novel perspective on CS-EGR in shale and further deepens the understanding of CS-EGR in shale reservoirs.

2 Numerical model description

In this work, the simulated reservoir represents the WL shale as observed from a shale gas exploration well (Well-WQ2) located in north-eastern Sichuan Basin at the intersection of Sichuan Province, Shaanxi Province, Hubei Province and Chongqing municipality (Fig. 1(a)). In this region, the geological background is complicated, as described in previous works in detail (Liu et al., 2016; Liu et al., 2017a; Shan et al., 2017; Zhao et al., 2020). Basically, the thickness of the WL shales is approximately 100 m (in which the Wufeng Formation occupies ~10 m), and the WL shales are located in the burial depth range of 1200–1300 m, according to the drilling and logging information. Accordingly, the depleted pressure is estimated to be approximately 1.7 MPa (Zhang et al., 2015). Moreover, strong vertical heterogeneity of many of the WL shale reservoir parameters (Liu et al., 2017a; Zhang et al., 2018), including permeability, porosity, Poisson's ratio, Young's modulus and Langmuir volume/pressure, is observed (Table 1).

Referring to a typical IW-PW arrangement (Li and Elsworth, 2019), the simulation model contains one IW in the center and four PWs in the corners, which is an axisymmetric pattern in geometric space (Fig. 1(b)). A two-dimensional section is selected for this simulation work, in which the anisotropic permeability is considered, and each layer is embedded with the particular parameters shown in Table 1, ensuring that the simulated reservoir reflects the real WL shales as accurately as possible (Fig. 1(b)). To avoid the potential influence from the right boundary (Li et al., 2017), for example, the influence of formation overpressure, the width of the model reservoir is set to 300 m. Herein, the 100 m × 300 m rectangular area is divided into 5085 elements, where the gas pressure at the

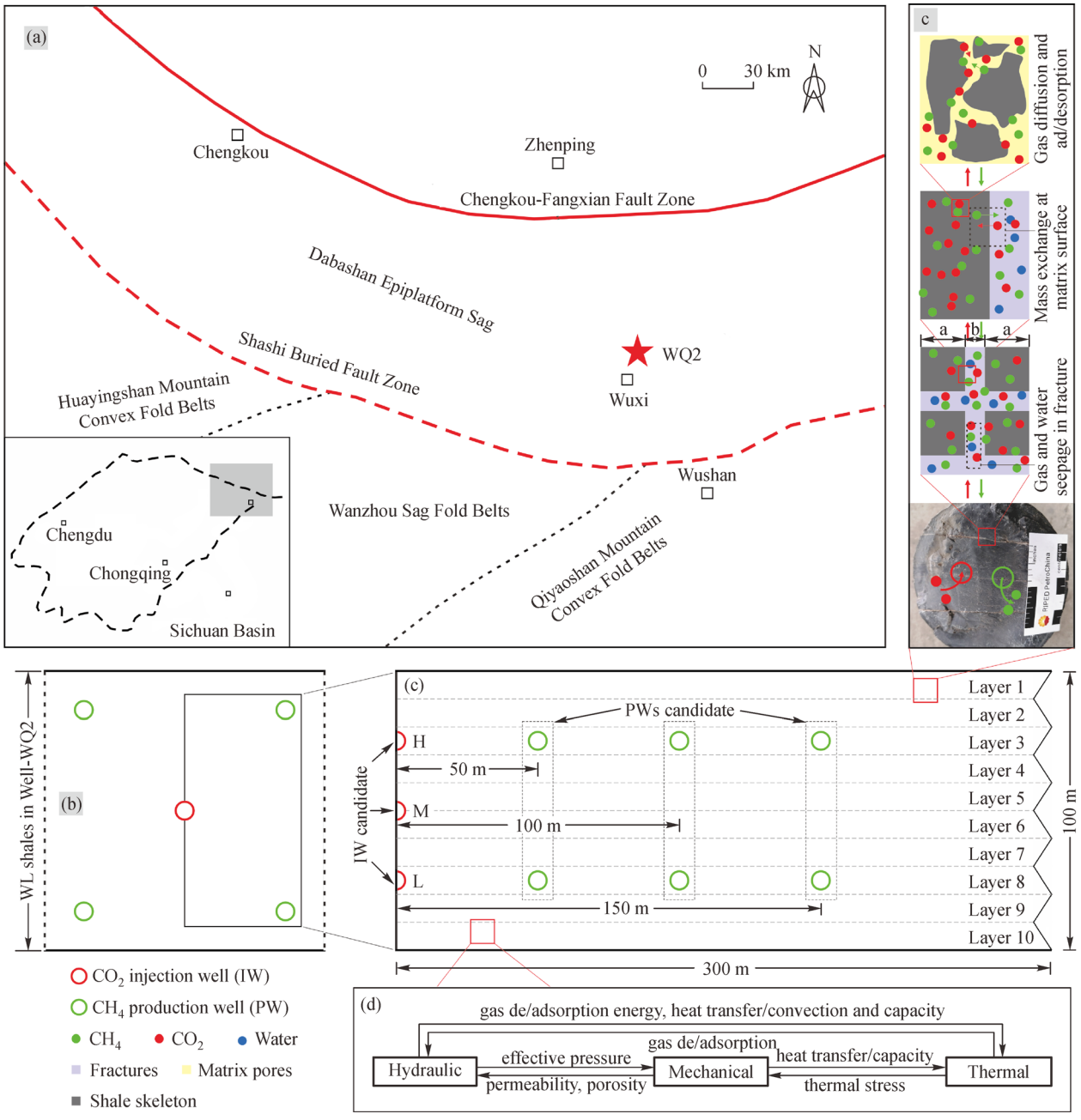

Fig. 1 Schematic diagram of the geological settings, model description and THM coupling process (Liu et al., 2017a; Zhao et al., 2020). (a) regional overview of Well-WQ2; (b) schematic diagram of the IW and PWs; (c) the dual-porosity modeling system; (d) THM coupling relations.

right boundary is set as the initial gas pressure and the rest of the boundaries do not allow flux. For this simulation work, the temperature is 305 K, the initial pressure of the CO_2 and CH_4 is 0.3 MPa and 1.7 MPa (same as the depleted pressure), respectively. During CS-EGR, a constant pressure of 7 MPa and 0.1 MPa is applied to the IW and the PWs, respectively. Other basic parameters (Table 2) adopted in this numerical work refer to existing work (Sun et al., 2013; Fathi and Akkutlu, 2014; Li and Elsworth, 2015; Fan et al., 2019a; Fan et al., 2019b; Li and Elsworth, 2019; Guo et al., 2020a; Liu et al., 2020; Zhao et al., 2020).

Based on the simulated reservoir, nine IW-PW combinations are studied to determine how the relative locations of IW and PWs affect the dynamic interaction of multiphase CH_4 during CO_2-enhanced gas recovery from depleted WL shales. When the IW targets the lower layer and has a horizontal distance from the PWs of 50 m, this case is

Table 1 Vertical heterogeneity of the WL shales at Well-WQ2

Layer No.	Depth/m	E/GPa	$v/10^{-1}$	φ/%		$K/(10^{-18}\ m^2)$		$V_L/(m^3 \cdot t^{-1})$		P_L/MPa	
				φ_m	φ_f	k_h	k_v	$V_{L\text{-}CH_4}$	$V_{L\text{-}CO_2}$	$P_{L\text{-}CH_4}$	$P_{L\text{-}CO_2}$
1	1200–1210	44.4	2.27	3.54	0.51	4.2	1.44	1.26	10.68	4.12	10.68
2	1210–1220	45.6	2.7	2.78	0.32	1.82	0.72	1.57	8.75	3.84	8.75
3	1220–1230	51.5	2.52	2.07	0.43	3.2	1.1	1.57	8.69	3.58	8.69
4	1230–1240	63.8	2.08	2.84	0.66	4.6	0.86	2.46	9.5	3.04	9.5
5	1240–1250	62.4	2.13	1.36	0.44	1.68	0.58	2.17	11.75	2.28	11.75
6	1250–1260	60.7	2.19	2.88	0.42	6.4	2.06	2.01	8.79	3.16	8.79
7	1260–1270	60.9	2.18	1.72	0.53	5	1.14	2.78	13.99	2.6	13.99
8	1270–1280	61.3	2.17	5.54	0.66	8.1	2.11	2.49	10.09	3.21	10.09
9	1280–1290	58.6	2.26	1.26	0.51	3.8	1.28	3.01	9.11	2.87	9.11
10	1290–1300	57.8	2.29	2.59	0.78	3.6	1.36	3.59	6.01	4.01	6.01

Note: E—Young's modulus; v—Poisson's ratio; φ—Porosity; φ_f—Fracture porosity; φ_m—Matrix porosity; k—Permeability; k_h—Horizontal permeability; k_v—Vertical permeability; V_L—Langmuir volume; P_L—Langmuir pressure

Table 2 Key parameters for CS-EGR in this numerical simulation

Parameter	Value	Parameter	Value
Langmuir strain coefficient of CH_4 (ε_{L1})	8.1e-4	Endpoint relative permeability of gas (k_{rg0})	0.875
Langmuir strain coefficient of CO_2 (ϵ_{L2})	3.6e-3	Endpoint relative permeability of water (k_{rw0})	1.0
Dynamic viscosity of CH_4 (μ_{g1}, Pa·s)	1.34e-5	Biot coefficient of matrix (α_m)	0.8
Dynamic viscosity of CO_2 (μ_{g2}, Pa·s)	1.84e-5	Biot coefficient of fracture (α_f)	0.1
Dynamic viscosity of water (μ_w, Pa·s)	8.9e-4	Density of the shale skeleton (ρ_c, kg/m^3)	2470
Diffusion coefficient of CH_4 (D_1, m^2/s)	3.6e-12	Initial fracture width (b, m)	5e-4
Diffusion coefficient of CO_2 (D_2, m^2/s)	5.8e-12	Initial fracture stiffness (K_{nj}, GPa/m)	10
Thermal coefficient of gas sorption (c_1, 1/K)	0.021	Maximum fracture aperture (Δv_{max}, m)	0.001
Thermal coefficient of gas sorption (c_2, 1/MPa)	0.071	Thermal expansion coefficient (α_T, 1/K)	2.4e-5
Capillary pressure (p_{cgw}, MPa)	0.035	Specific heat capacities of shale (C_s, J/(kg·K))	1380
Initial density of saturated vapor (ρ_{fv0}, kg/m^3)	0.13	Specific heat capacities of CH_4 (C_{g1}, J/(kg·K))	2220
Latent heat of vapor (R_v, J/(K·kg))	461.51	Specific heat capacities of CO_2 (C_{g2}, J/(kg·K))	844
Klinkenberg factor (b_k, MPa)	0.76	Specific heat capacities of water (C_w, J/(kg·K))	4187
Desorption time of CH_4 (τ_1, d)	0.221	Specific heat capacities of vapor (C_v, J/(kg·K))	1996
Desorption time of CO_2 (τ_2, d)	0.334	Thermal conduction coefficient of shale (λ_s, W/(m·K))	0.1913
Henry's coefficient of CH_4 (H_{g1})	0.0014	Thermal conduction coefficient of CH_4 (λ_{g1}, W/(m·K))	0.0301
Henry's coefficient of CO_2 (H_{g2})	0.0347	Thermal conduction coefficient of CO_2 (λ_{g2}, W/(m·K))	0.0137
Residual gas saturation (s_{gr})	0.05	Thermal conduction coefficient of water (λ_w, W/(m·K))	0.5985
Irreducible water saturation (s_{wr})	0.42	Isosteric heat of CH_4 adsorption (q_{st1}, kJ/mol)	16.4
Reference temperature for test (T_{ref}, K)	300	Isosteric heat of CO_2 adsorption (q_{st2}, kJ/mol)	19.2

labeled L50. Similarly, the remaining cases are L100, L150, M50, M100, M150, H50, H100 and H150 (Fig. 1(b)). Herein, the operation conditions for all cases are identical, except the IW-PWs locations. In this work, the candidate IW is only set in layer 3, the transition zone of layers 5–6, and layer 8 to represent the upper, middle and lower shale reservoirs, respectively. In addition, for each simulated case, the CS-EGR operation is independent, and the continuous run time is set to 10000 days (approximately 30 years).

3 THM coupling process and governing equations

Referring to previous achievements based on numerical

works (Vega et al., 2014; Hu et al., 2019; Li and Elsworth, 2019), the simulated shale reservoir is treated as a dual-porosity medium (Fig. 1(c)). In this dual-porosity medium, the injection of CO_2 tends to activate a very complicated process due to a series of feedbacks controlled by the THM coupling effect, as exhibited by Fig. 1(d). Basically, the pivotal equations involved in the numerical modeling of this work refer to previous achievements (Fan et al., 2019a; Fan et al., 2019b; Li and Elsworth, 2019; Zhang et al., 2020; Zhao et al., 2020), mainly describing the following seven aspects

I. Mechanical field:

$$Gu_{k,ll}+\frac{G}{1-2\nu}u_{l,lk}-\left(\alpha_{\mathrm{m}}p_{\mathrm{m},k}+\alpha_{\mathrm{f}}p_{\mathrm{f},k}\right)-K\alpha_{\mathrm{T}}T_k$$

$$-K\left(\frac{\varepsilon_{L1}b_1p_{\mathrm{mg1}}+\varepsilon_{L2}b_2p_{\mathrm{mg2}}}{1+b_1p_{\mathrm{mg1}}+b_2p_{\mathrm{mg2}}}\right)_{,k}+f_k=0, \tag{1}$$

where the subscript i represents the gas component (1 for CH_4 and 2 for CO_2); u_k is the deformation in the k direction; $G=E/(2+2\nu)$ is the shear modulus, Pa; $K=E/3(1-2\nu)$ is the bulk modulus, Pa; E is Young's modulus, Pa; ν is Poisson's ratio; α_{m} and α_{f} are the Biot effective stress coefficients of the matrix and fracture, respectively; p_{m} is the total gas pressure in the matrix, Pa; $p_{\mathrm{mg}i}$ is the gas pressure in the pore system, Pa; p_{f} is the fluid stress in the fracture, Pa; α_{T} is the thermal expansion coefficient, $1/K$; T is the temperature of gas, K; $b_i=1/P_{\mathrm{L}i}$; $P_{\mathrm{L}i}$ is the Langmuir pressure constant, Pa; $\varepsilon_{\mathrm{L}1}$ and $\varepsilon_{\mathrm{L}2}$ are the Langmuir strain coefficients of CH_4 and CO_2; and f_k is the volume force component, N.

II. Hydraulic field:

$$\frac{\partial}{\partial t}\left(\varphi_{\mathrm{m}}\frac{M_{\mathrm{g}i}}{RT}p_{\mathrm{mg}i}+\frac{V_{Li}b_ip_{\mathrm{mg}i}}{1+b_1p_{\mathrm{mg1}}+b_2p_{\mathrm{mg2}}}\rho_c\rho_{\mathrm{gs}i}\right.$$

$$\left.\exp\left(-\frac{c_1}{1+c_2p_{\mathrm{m}}}(T-T_{\mathrm{ref}})\right)+\nabla\cdot\left(-D_iM_{\mathrm{g}i}\nabla\varphi_{\mathrm{m}}\frac{p_{\mathrm{mg}i}}{RT}\right)\right)$$

$$=-\frac{1}{\tau_i}\frac{M_{\mathrm{g}i}}{RT}\left(p_{\mathrm{mg}i}-p_{\mathrm{fg}i}\right), \tag{2}$$

where $M_{\mathrm{g}i}$ is the gas molar mass, g/mol; φ_{m} is the porosity of the shale matrix; R is the gas molar constant, J/(mol·K); ρ_{c} is the density of the shale skeleton, kg/m^3; $\rho_{\mathrm{gs}i}$ is the gas density under standard conditions, kg/m^3; $p_{\mathrm{fg}i}$ is the gas pressure in the fracture system, Pa; $V_{\mathrm{L}i}$ is the Langmuir volume constant, m^3/kg; c_1 and c_2 are the thermal coefficients of gas sorption; D_i is the diffusion coefficient, m^2/s; T_{ref} is the reference temperature, K; and τ_i is the desorption time, s.

$$\frac{\partial(s_{\mathrm{g}}\varphi_{\mathrm{f}}\rho_{\mathrm{fg}i})}{\partial t}+\nabla\cdot\left(-\rho_{\mathrm{fg}i}\frac{kk_{\mathrm{rg}}}{\mu_{\mathrm{g}i}}\left(1+\frac{b_{\mathrm{k}}}{p_{\mathrm{fg}i}}\right)\nabla p_{\mathrm{fg}i}\right)$$

$$+\frac{\partial(s_{\mathrm{w}}\varphi_{\mathrm{f}}H_{\mathrm{g}i}\rho_{f\mathrm{g}i})}{\partial t}+\nabla\cdot\left(-H_{\mathrm{g}i}\rho_{\mathrm{fg}i}\frac{kk_{\mathrm{rw}}}{\mu_{\mathrm{w}}}\nabla p_{\mathrm{fw}}\right)$$

$$=\frac{1}{\tau_i}\frac{M_{\mathrm{g}i}}{RT}\left(p_{\mathrm{mg}i}-p_{\mathrm{fg}i}\right), \tag{3}$$

$$\frac{\partial(s_{\mathrm{w}}\varphi_{\mathrm{f}}\rho_{\mathrm{w}})}{\partial t}+\nabla\cdot\left(-\rho_{\mathrm{w}}\frac{kk_{\mathrm{rw}}}{\mu_{\mathrm{w}}}\nabla p_{\mathrm{fw}}\right)$$

$$+\frac{\partial}{\partial t}\left(s_{\mathrm{g}}\varphi_{\mathrm{f}}\rho_{\mathrm{fv0}}\exp\left(\frac{p_{\mathrm{cgw}}}{\rho_{\mathrm{w}}R_{\mathrm{v}}T}\right)\right)+$$

$$\nabla\cdot\left(-\rho_{\mathrm{fv0}}\exp\left(\frac{p_{\mathrm{cgw}}}{\rho_{\mathrm{w}}R_{\mathrm{v}}T}\right)\sum_{i=1}^{2}\right.$$

$$\left.\frac{kk_{\mathrm{rg}}}{\mu_{\mathrm{g}i}}\left(1+\frac{b_{\mathrm{k}}}{p_{\mathrm{fg}i}}\right)\nabla p_{\mathrm{fg}i}\right)=0, \tag{4}$$

where φ_{f} is the fracture porosity; s_{g} is the gas saturation; $s_{\mathrm{w}}=1-s_{\mathrm{g}}$ is the water saturation; $\rho_{\mathrm{fg}i}$ is the gas density, kg/m^3; $H_{\mathrm{g}i}$ is Henry's coefficient of gas; k is the absolute permeability, m^2; k_{rg} and k_{rw} are the relative permeabilities of the gas and water; $\mu_{\mathrm{g}i}$ and μ_{w} are the dynamic viscosities of the gas and water, Pa·s; b_{k} is the Klinkenberg factor, Pa; $p_{\mathrm{fw}}=p_{\mathrm{fg}}-p_{\mathrm{cgw}}$ is the water pressure in the fracture, Pa; p_{fg} is the total gas pressure in the fracture, Pa; p_{cgw} is the capillary pressure, Pa; ρ_{w} is the density of water, kg/m^3; ρ_{fv0} is the density of saturated vapor, kg/m^3; R_v is the latent heat of vapor, J/(K·kg); s_{gr} is the residual gas saturation; and s_{wr} is the irreducible water saturation.

III. Thermal field:

$$\frac{\partial}{\partial t}\left((\rho C_p)_{\mathrm{eff}}T\right)+\eta_{\mathrm{eff}}\nabla T-\nabla\cdot(\lambda_{\mathrm{eff}}\nabla T)+K\alpha_{\mathrm{T}}T\frac{\partial\varepsilon_{\mathrm{V}}}{\partial t}$$

$$+\sum_{i=1}^{2}q_{\mathrm{st}i}\frac{\rho_{\mathrm{s}}\rho_{\mathrm{gs}i}}{M_{\mathrm{g}i}}\frac{\partial V_{\mathrm{sg}i}}{\partial t}=0, \tag{5}$$

where $(\rho C_{\mathrm{p}})_{\mathrm{eff}}$ is the effective heat capacity, J/(m^3·K); η_{eff} is the effective heat convection transfer coefficient, J/(m^2·s); λ_{eff} is the effective thermal conductivity, W/(m·K); $q_{\mathrm{st}i}$ is the isosteric heat of gas adsorption, kJ/mol; ε_{V} is the volume strain; and $V_{\mathrm{sg}i}$ is the absorbed gas content, m^3/kg.

IV. Matrix porosity:

$$\varphi_{\mathrm{m}}=\varphi_{\mathrm{m0}}+\frac{(\alpha_{\mathrm{m}}-\varphi_{\mathrm{m0}})(\varepsilon_{\mathrm{e}}-\varepsilon_{\mathrm{e0}})}{1+\varepsilon_{\mathrm{e}}}, \tag{6}$$

where $\varepsilon_{\mathrm{e}}=\varepsilon_{\mathrm{v}}+p_{\mathrm{m}}/K_{\mathrm{s}}-\alpha_T T-\varepsilon_{\mathrm{s}}$; and the subscript 0 represents the initial value of the parameters.

V. Fracture porosity:

$$\varphi_{\mathrm{f}} = \varphi_{\mathrm{f0}}\left(1+\frac{\sum_{j=1}^{N}\Delta b_j}{\sum_{j=1}^{N} b_{j0}}\right) = \varphi_{\mathrm{f0}}\left(1+\frac{\sum_{j=1}^{N}\left(\Delta\sigma_{\mathrm{n}j}-\alpha_{\mathrm{f}}\Delta p_{\mathrm{f}}\right)/\left(K_{\mathrm{n}j}\left(1-\frac{\sigma'_{\mathrm{n}j}}{K_{\mathrm{n}j}\Delta v_{\max}+\sigma'_{\mathrm{n}j}}\right)^{-2}\right)}{\sum_{j=1}^{N} b_{j0}}\right), \quad (7)$$

where the subscript j represents the direction; $\Delta\sigma_{\mathrm{n}j}$ is the normal stress on the fracture, Pa; $K_{\mathrm{n}j}$ is the initial normal stiffness, Pa/m; $\sigma_{\mathrm{n}j}$ is the normal effective stress, Pa; $\Delta v_{\max}$ is the maximum fracture aperture as applied normal effective stress goes to infinity, m; b_{j0} is the initial fracture width, m; and N represents the dimension – for two dimensions $N = 2$, and for three dimensions $N = 3$.

VI. Permeability evolution

$$k_j = k_{j0}\left(1+\frac{\Delta b_j}{b_{j0}}\right)^3, \quad (8)$$

where Δb_j is the change of the fracture width, m.

VII. Relative permeability

$$k_{\mathrm{rg}} = k_{\mathrm{rg0}}\left(1-\left(\frac{s_{\mathrm{w}}-s_{\mathrm{wr}}}{1-s_{\mathrm{gr}}-s_{\mathrm{wr}}}\right)\right)^2\left(1-\left(\frac{s_{\mathrm{w}}-s_{\mathrm{wr}}}{1-s_{\mathrm{wr}}}\right)^2\right), \quad (9)$$

$$k_{\mathrm{rw}} = k_{\mathrm{rw0}}\left(\frac{s_{\mathrm{w}}-s_{\mathrm{wr}}}{1-s_{\mathrm{wr}}}\right)^4, \quad (10)$$

where k_{rg0} and k_{rw0} are the endpoint relative permeabilities of the gas and water, respectively; s_{gr} is the residual gas saturation; and s_{wr} is the irreducible water saturation.

4 Results and discussion

Depending on the rigorous model, this work outputs the multiphase CH_4 content in the depleted WL shales just before external CO_2 is injected into the reservoir. Then, after CO_2 is injected, how the free CH_4 and adsorbed CH_4 dynamically vary during the CS-EGR process is explored. Following this issue, the influence of relative IW-PWs locations on the resulting interaction of multiphase CH_4 is also clarified. On this basis, this work further discusses the implications for CO_2-enhanced gas recovery in depleted WL shales. In addition, it should be noted that the thickness of the simulated reservoir is set to 1 m when the free/adsorbed CH_4 content is calculated.

4.1 Original characteristics of multiphase CH_4 before CO_2 involvement

Controlled by the heterogeneous parameters shown in Table 1, the residual content of CH_4 in each layer of depleted WL shales differs (Fig. 2), where the content of the adsorbed CH_4 is mainly determined by the reservoir pressure and Langmuir volume/pressure, while that of the free CH_4 is calculated based on the reservoir pressure and fracture/matrix porosity. With regard to the total CH_4 content in the depleted WL shales, the greatest content of residual CH_4 occurs in the layer at a depth of ~1275 m (layer 8) and is ~4604 kg, which is roughly two times the residual content (~2334 kg) of CH_4 in the layer at ~1225 m (layer 3). By contrast, the adsorbed CH_4 tends to occupy a greater proportion than the free CH_4 (excluding the situation in layer 1), where the average percentages of adsorbed CH_4 and free CH_4 are ~71% and ~29%, respectively (Fig. 2). Nevertheless, the proportion of multiphase CH_4 is variable among the layers with different burial depths, and the deeper layer generally has a higher proportion of adsorbed CH_4 in the total residual CH_4 (Fig. 2).

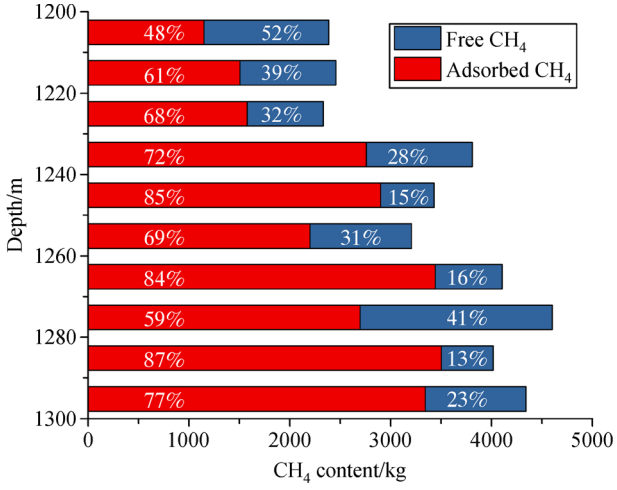

Fig. 2 Original content of multiphase CH_4 in each layer before CO_2 injection.

In particular, the situation of multiphase CH_4 in the depleted WL shales exhibits the following rules: 1) the Langmuir pressure/volume determines the content of adsorbed CH_4, and 2) the matrix/fracture porosity controls the content of free CH_4, under the condition that all layers in the vertical profile exhibit the same depleted pressure, before CO_2 injection. Therefore, in the depleted WL shales, the original contents of the CH_4 phases in the multiphase CH_4 are independent; in other words, the original content and proportion of adsorbed CH_4 shows no relationship with those of free CH_4 (Fig. 2). It seems almost inevitable that the vertical variability in the content/proportion of multiphase CH_4 among the layers, resulting from the CO_2-CH_4 displacement that occurs when the

injected CO_2 enters the layers at different times, tends to increase the complexity of the dynamic interaction between adsorbed CH_4 and free CH_4.

4.2 Dynamic variation in multiphase CH_4 during the CS-EGR process

Current knowledge supports that the CH_4 content in shale reservoirs decreases after CO_2 is injected (Sun et al., 2013; Iddphonce et al., 2020; Klewiah et al., 2020; Zhao et al., 2020). Herein, the dynamic decrease in the free CH_4 and adsorbed CH_4 during 10000 days of CS-EGR is obtained from this simulation work. As shown in Fig. 3, the decrease in multiphase CH_4 is activated by CO_2 injection and increases with time in the process of CS-EGR in WL shales. Meanwhile, the decrease in adsorbed CH_4 is always greater than that in free CH_4 during the CO_2-CH_4 displacement for all IW-PW combinations. Nevertheless, in the whole WL shale, the decreases in adsorbed CH_4 and free CH_4 differ due to the different IW-PWs arrangements. For example, case H50 (Fig. 3(a)) allows more CH_4 to be driven out from the WL shales than case M150 (Fig. 3(b)).

During the decrease in the free CH_4 content in the WL shales after CO_2 injection, the reduction in multiphase CH_4 varies with time. Basically, this variation is j a two-step process, with a dynamic stage (Stage I) and stable stage (Stage II), illustrated by the two representative cases (Fig. 4). In the early phase, the sudden injection of CO_2 forces the CH_4 that is originally in the adsorbed phase to convert to free CH_4, and the CH_4 released from the PWs is limited due to the short extraction time, together enabling the relative proportion of the decrease in adsorbed CH_4 to increase and that of free CH_4 to decrease, i.e., Stage I. Furthermore, the CO_2-CH_4 displacement occurs in a larger area with continued CO_2 migration, exhibiting a dynamic change with the continual decrease in free CH_4 at the PWs, resulting in the decrease in a stable proportion of free/adsorbed CH_4 among the total CH_4 during the continuous CO_2 injection into the WL shales, i.e., Stage II. By contrast, Stage I tends to cover a longer period with a

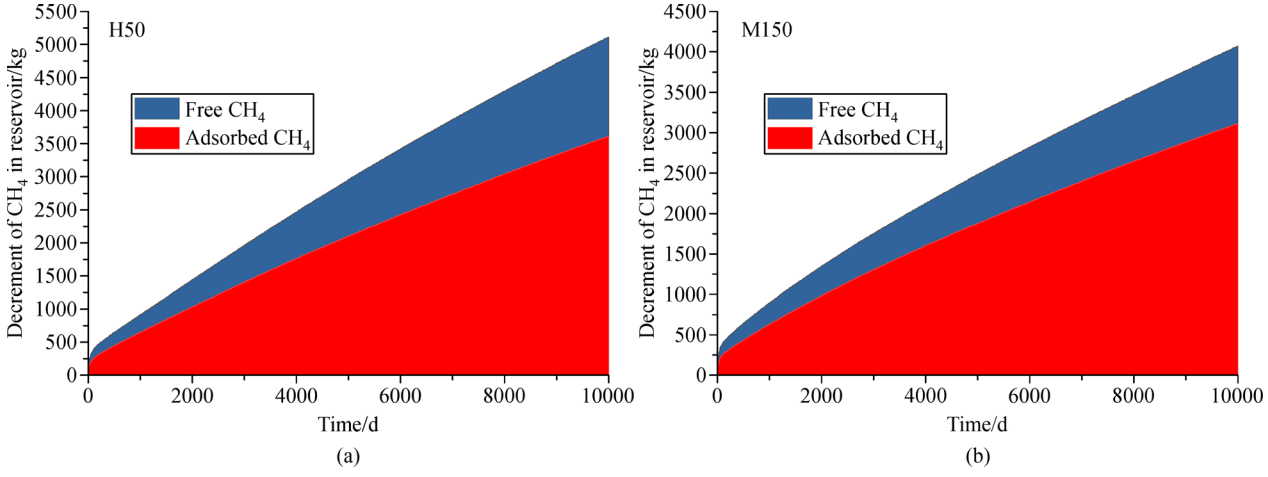

Fig. 3 Dynamic decrement of multiphase CH_4 in representative cases (a) H50 and (b) M150.

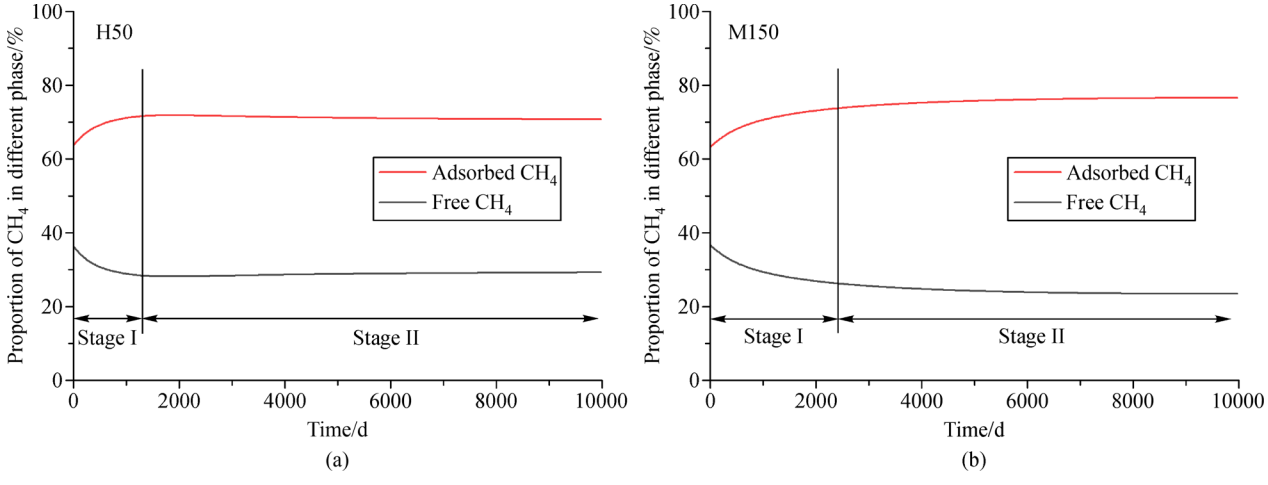

Fig. 4 Variation in the rate of decrease in multiphase CH_4 during the CS-EGR process of representative cases (a) H50 and (5) M150.

longer IW-PWs distance (Fig. 4). In this work, according to statistics, the resulting proportions of adsorbed CH_4 among all the extracted CH_4 under different IW-PWs combinations are similar (that is, 70%–80%).

With the decrease in CH_4 caused by CO_2 injection, the proportion of the residual multiphase CH_4 in the WL shales varies dynamically. Figure 5 shows that the relative IW-PWs location significantly affects the variation in the proportion of free CH_4 in the modeling reservoir. For the "50" series (H50, M50 and L50), the proportion of free CH_4 first slowly increases and then decreases linearly with CO_2 injection because the insufficient CO_2-CH_4 displacement due to limited CO_2 migration (a short IW-PW distance) is unable to compensate for the free CH_4 released from the PWs. With regard to the "150" series (H150, M150 and L150), CO_2-CH_4 displacement occurs in a large area (a long IW-PW distance) and thus generates massive free CH_4 that is converted from the adsorbed CH_4, overshadowing the free CH_4 extraction from the PWs, ultimately enabling a roughly linear increase in the proportion of residual free CH_4 in the WL shales. For the "100" series (H100, M100 and L100), the results are between those of the "50" series and the "150" series, suggesting a Langmuir-like variation in the proportion of residual free CH_4, which first increases and then tends to be stable (Fig. 5).

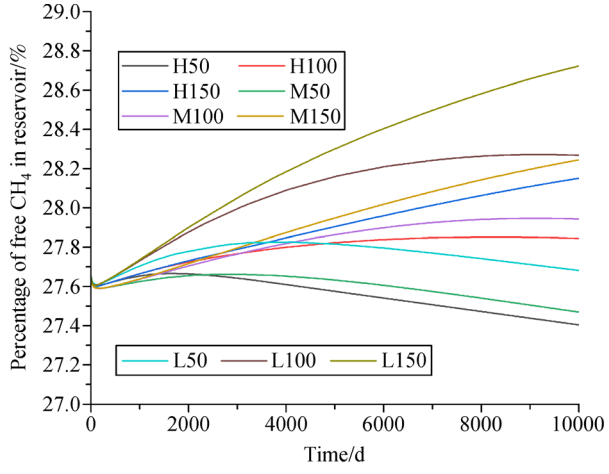

Fig. 5 Percentage variation of free CH_4 in whole reservoir of each operation condition.

In addition, adsorbed CH_4 exists on the surface of the shale skeleton, while free CH_4 appears in both the fractures and the matrix pores in this dual-porosity system of modeling shale reservoirs (Fan et al., 2019a; Li and Elsworth, 2019). Accordingly, it is meaningful to discuss the dynamic variation in free CH_4 in fractures and matrix pores, helping enhance the understanding of the change in free CH_4 during the shale-based CS-EGR process. Generally, CO_2 injection enables a roughly linear decline in the free CH_4 content in both fractures and matrix pores (Fig. 6). Therein, the content of free CH_4 in the matrix pores is always greater than that in the fractures, controlled by the fact that φ_f is less than φ_m (Table 1). However, Fig. 6 also states that the ratio of the free CH_4 in the fractures to that in the matrix pores differs during CS-EGR operation under variable IW-PWs combinations. According to Fig. 7, the variation range of the relative content of CH_4 in the fractures to that in the matrix pores is not significant and is only between 12.1% and 12.6%. To describe this phenomenon in detail, the variation in this ratio (see Fig. 7) can be divided into three types, corresponding to the "50" series, "100" series and "150" series, where the change law is similar to that shown in Fig. 5.

4.3 Outputs of multiphase CH_4 after 10000 d of CO_2 injection

The vertical nonuniform distribution of multiphase CH_4 in the modeling reservoir, accompanied by the complex/dynamic variation in multiphase CH_4 during CS-EGR operation, varies the outputs of multiphase CH_4 after

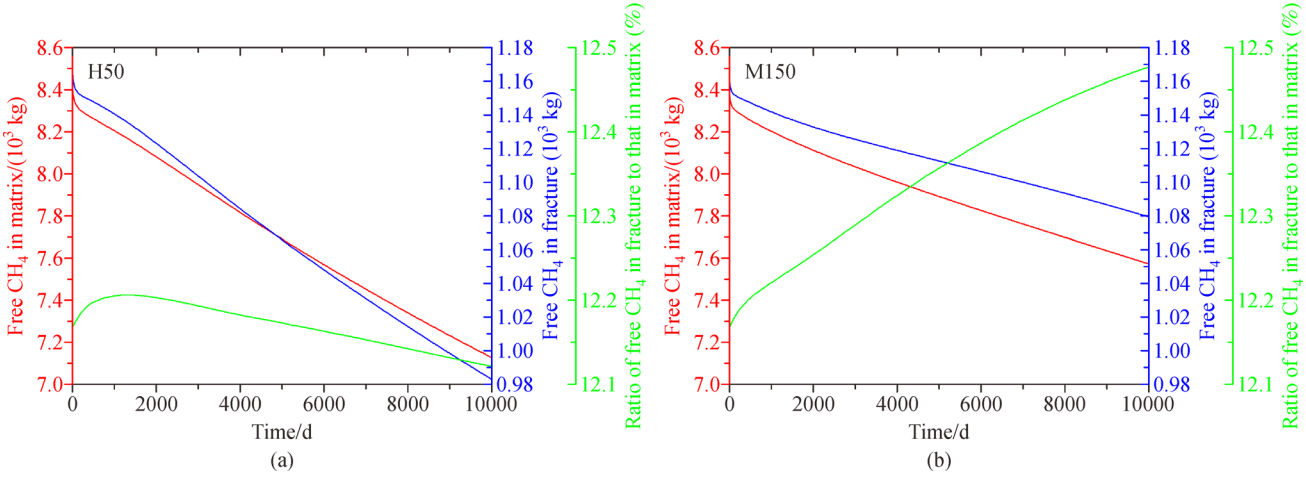

Fig. 6 Dynamic variation of free CH_4 in the matrix and in the fracture of representative cases (a) H50 and (b) M150.

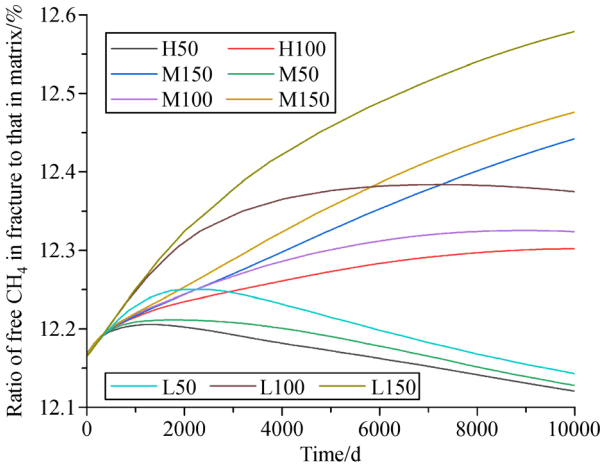

Fig. 7 Relative content of CH_4 in the fracture to that in the matrix during the CS-EGR process for each operation case.

10000 d of CO_2 injection under nine IW-PWs combinations. For example, the residual adsorbed CH_4, the residual free CH_4 and their ratio (relative content) resulting from case H50 (Fig. 8(a)) are totally different from those resulting from case M150 (Fig. 8(b)). Nevertheless, regardless of where the IW and PWs are located, the adsorbed CH_4 content is always higher than the free CH_4 content (Fig. 8) throughout the process of CO_2-enhanced shale gas recovery from the WL shales. This phenomenon is determined by the reservoir parameters, even though the local pressure of the modeling reservoir is variable after CO_2 injection (Zhao et al., 2020).

In fact, the residual CH_4 content in the whole reservoir (or in each layer) is the difference between the original CH_4 content and the decreased CH_4 content in the whole reservoir (or in each layer). Thus, in this work, the final decrease in multiphase CH_4 is introduced to analyze the CS-EGR outcomes in the whole modeling reservoir or in each independent layer. The resulting decrease in free/adsorbed CH_4 under different IW-PW combinations differs (Fig. 9), revealing the significance of IW-PWs location in shale-based CS-EGR operation. Briefly, the vertical variability in the decrease in free/adsorbed CH_4 is strong, but a gradual increasing tendency roughly exists with burial depth (Fig. 9). For all the IW-PWs combinations, the bottom layer, with the most favorable sections for in situ shale gas development (Liu et al., 2017a), is the main contributors to the CH_4 recovery during the CS-EGR progress. According to Fig. 9, for every layer, a shorter IW-PW distance enables a greater decrease in CH_4 in the WL shales, in which the proportion of adsorbed CH_4 is lower, and vice versa. In addition, when the PWs are fixed, it seems that the IW location only slightly affects the decrease in CH_4 and the corresponding ratio of the adsorbed/free CH_4.

4.4 Implications for CO_2 enhanced shale gas recovery

From the perspective of the whole modeling reservoir, the injection of CO_2 partly recovers the residual CH_4 from the depleted WL shales (Fig. 10). When the IW location is fixed, the "150" series cases (H150, M150 and L150) have more CH_4 remaining in the reservoirs, lowering the corresponding proportion of adsorbed CH_4 relative to all the residual CH_4 in the WL shales (Fig. 10). That is, the "50" series generates a greater content of recovered CH_4 (only cases H50, M50 and L50 have CH_4 recoveries of more than 5000 kg), while the "150" series is not beneficial for CO_2 shale gas recovery (cases H150, M150 and L150 force only ~4000 kg CH_4 to be recovered) after 10000 d of CS-EGR operation in the WL shales (Fig. 11(a)). Moreover, under different IW-PW combinations, although the total recovered CH_4 contents differ, the proportions of adsorbed CH_4 relative to all the recovered CH_4 are close and vary in the range of 75%–78% (Fig. 11(a)).

Comparing the residual CH_4 contents in the WL shales before and after 10000 d CO_2 injection, the shale gas recovery efficiency is obtained (Fig. 12). Influenced by the variable interaction of multiphase CH_4 after CO_2 is

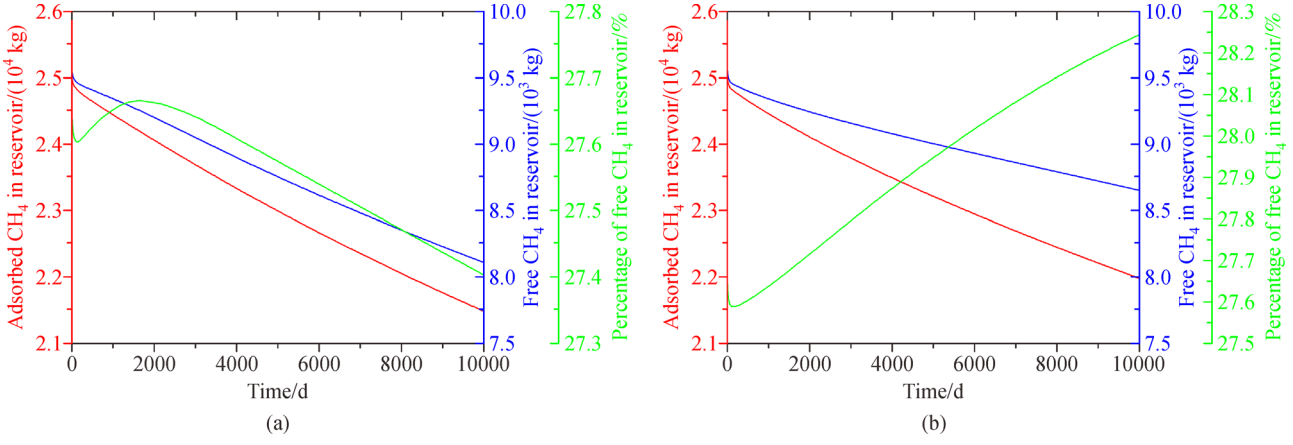

Fig. 8 Residual content of multiphase CH_4 in the whole reservoir of representative cases (a) H50 and (b) M150.

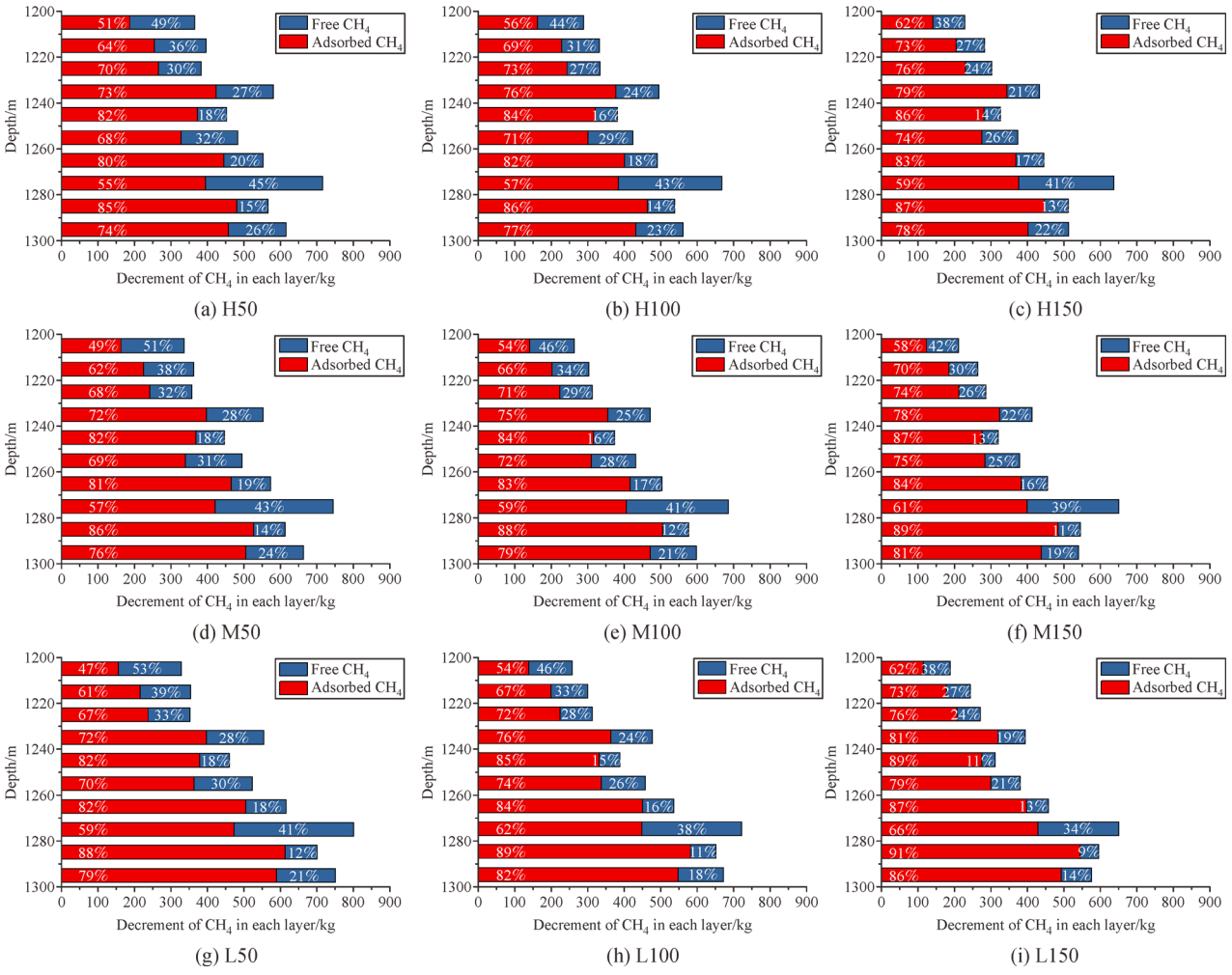

Fig. 9 Decrease in multiphase CH_4 from each layer in all simulation cases after 10000 d of CS-EGR operation.

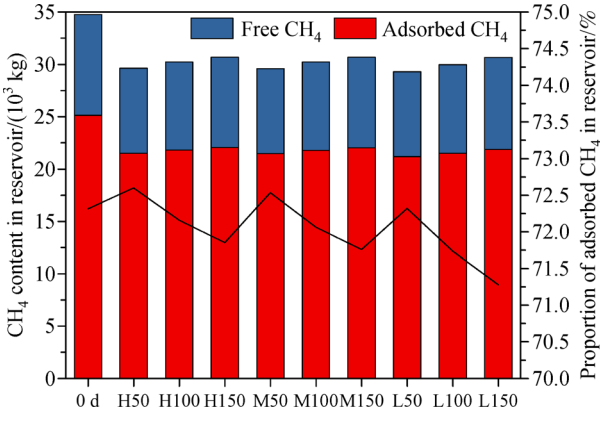

Fig. 10 Final residual CH_4 in whole reservoir under each IW-PWs combination at the end of CS-EGR operation.

injected into the modeling reservoir, the resulting shale gas recovery efficiency is different under different IW-PWs combination. Basically, the efficiency of CO_2-enhanced shale gas recovery varies from 11% to 16%, with an average of 13.3%. Herein, the greatest efficiency of 15.6% emerges for case L50, while the lowest (~11.7%) corresponds to the "150" series (H150, M150 and L150) (Fig. 12). Accordingly, it could be speculated that a shorter IW-PWs distance is needed to obtain a higher efficiency of CO_2-enhanced shale gas recovery from the WL shales if the IW targets the bottom layer. Moreover, this speculation might be suitable for all the WL shales in the Sichuan Basin, assuming that the WL shales in the north-eastern Sichuan Basin are representative (Liu et al., 2017a; Su et al., 2007; Shan et al., 2017).

5 Conclusions

According to a novel numerical model with THM coupling and the measured reservoir parameters of the depleted WL shales located in the north-eastern Sichuan Basin, the dynamic variation in free CH_4 and adsorbed CH_4 during/after 10000 days of CS-EGR deployment is investigated

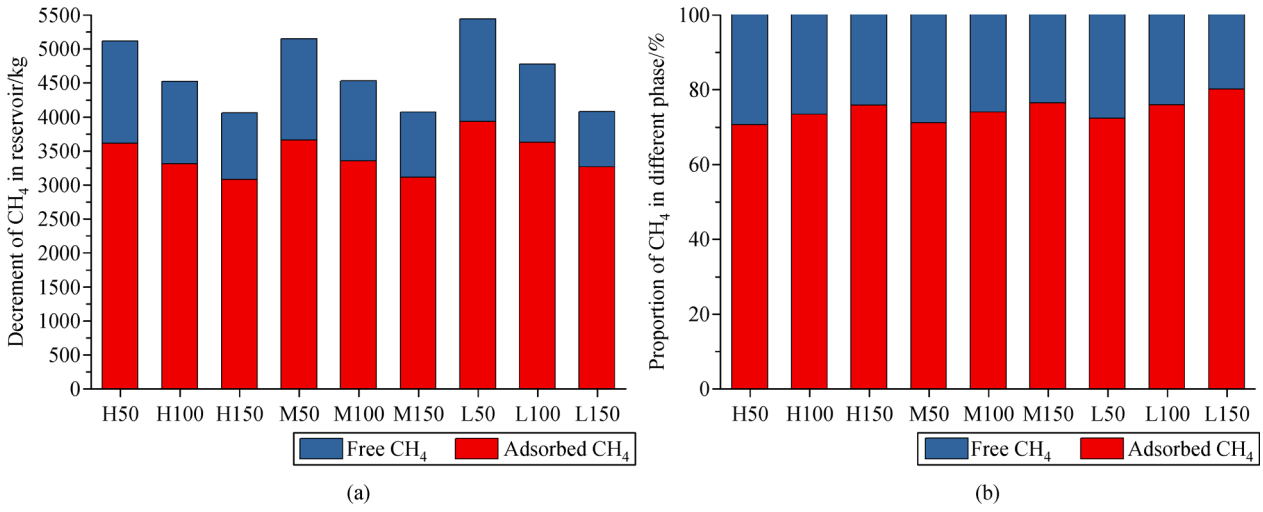

Fig. 11 Multiphase recovered CH_4 from the whole reservoir and the corresponding proportion of free/adsorbed CH_4.

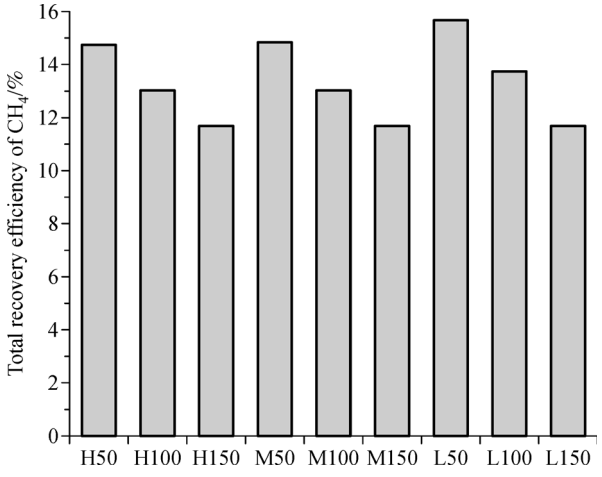

Fig. 12 Total recovery efficiency of multiphase CH_4 from whole reservoir under each IW-PWs combination.

under nine combinations of IW and PWs. The main conclusions are as follows.

1) As revealed by the numerical simulation, the residual CH_4 content in the depleted WL shales varies in the vertical direction, and the adsorbed CH_4 tends to occupy a greater proportion than the free CH_4. The residual CH_4 content and the corresponding ratio of adsorbed/free CH_4 vary in a complicated manner after CO_2 is injected into the shale reservoir.

2) For the decreased CH_4, this variation in the proportion of the multiphase CH_4 contains two stages, a dynamic stage and stable stage, in which the resulting proportions of adsorbed CH_4 among all extracted CH_4 phases under different IW-PWs combinations are similar (that is, 70%–80%).

3) The relative locations of the IW and PWs significantly affect the predicted CS-EGR outcomes in the WL shales, where the dynamic interaction of adsorbed CH_4 and free CH_4 differs under different IW-PWs combinations, resulting in the variable efficiency of CO_2-enhanced shale gas recovery. Basically, a shorter IW-PWs distance seems to be helpful in increasing the CH_4 recovery efficiency if the IW targets the bottom layer of the WL shales.

Acknowledgements This study was financially supported by the Project funded by China Postdoctoral Science Foundation (No. 2020M683253), the Key Laboratory of Shale Gas Exploration, Ministry of Natural Resources (No. KLSGE-MLR-202003), and the National Natural Science Foundation of China (Grant No. 51704197).

References

Abidoye L K, Khudaida K J, Das D B (2015). Geological carbon sequestration in the context of two-phase flow in porous media: a review. Crit Rev Environ Sci Technol, 45(11): 1105–1147

Chen B, Harp D R, Lu Z, Pawar R J (2020). Reducing uncertainty in geologic CO_2 sequestration risk assessment by assimilating monitoring data. Int J Greenh Gas Control, 94: 102926

Chi J, Ju B, Lyu G, Zhang X, Wang J (2017). A computational method of critical well spacing of CO_2 miscible and immiscible concurrent flooding. Pet Explor Dev, 44(5): 771–778

Cui J W, Zhu R K, Mao Z G, Li S X (2019). Accumulation of unconventional petroleum resources and their coexistence characteristics in Chang7 shale formations of Ordos Basin in central China. Front Earth Sci, 13(3): 575–587

Fan C, Elsworth D, Li S, Zhou L, Yang Z, Song Y (2019a). Thermo-hydro-mechanical-chemical couplings controlling CH_4 production and CO_2 sequestration in enhanced coalbed methane recovery. Energy, 173: 1054–1077

Fan C, Luo M, Li S, Zhang H, Yang Z, Liu Z (2019b). A thermo-hydro-mechanical-chemical coupling model and its application in acid fracturing enhanced coalbed methane recovery simulation. Energies, 12(4): 626

Fan Y, Deng C, Zhang X, Li F, Wang X, Qiao L (2018). Numerical study of CO_2-enhanced coalbed methane recovery. Int J Greenh Gas Control, 76: 12–23

Fathi E, Akkutlu I Y (2014). Multi-component gas transport and adsorption effects during CO_2 injection and enhanced shale gas recovery. Int J Coal Geol, 123: 52–61

Gao Z, Fan Y, Xuan Q, Zheng G (2020). A review of shale pore structure evolution characteristics with increasing thermal maturities. Advances in Geo-Energy Research, 4(3): 247–259

Guo C, Li R, Sun J, Wang X, Liu H (2020a). A review of gas transport and adsorption mechanisms in two-component methane-carbon dioxide system. Int J Energy Res, 44(4): 2499–2516

Guo C, Li R, Wang X, Liu H (2020b). Study on two component gas transport in nanopores for enhanced shale gas recovery by using carbon dioxide injection. Energies, 13(5): 1–21

Hou H H, Shao L Y, Li Y H, Li Z, Zhang W L, Wen H J (2018). The pore structure and fractal characteristics of shales with low thermal maturity from the Yuqia Coalfield, northern Qaidam Basin, northwestern China. Front Earth Sci, 12(1): 148–159

Hu S, Hu X, He L, Chen W (2019). A new material balance equation for dual-porosity media shale gas reservoir. Energy Procedia, 158: 5994–6002

Iddphonce R, Wang J, Zhao L (2020). Review of CO_2 injection techniques for enhanced shale gas recovery: prospect and challenges. J Nat Gas Sci Eng, 77: 103240

Klewiah I, Berawala D S, Alexander Walker H C, Andersen P Ø, Nadeau P H (2020). Review of experimental sorption studies of CO_2 and CH_4 in shales. J Nat Gas Sci Eng, 73: 103045

Li D, He Y, Zhang H, Xu W, Jiang X (2017). A numerical study of the impurity effects on CO_2 geological storage in layered formation. Appl Energy, 199: 107–120

Li J, Li B, Wang Z, Ren C, Yang K, Chen S (2020a). An anisotropic permeability model for shale gas recovery considering slippage effect and embedded proppants. Nat Resour Res, 29(5): 3319–3333

Li J, Lu S, Cai J, Zhang P, Xue H, Zhao X (2018). Adsorbed and free oil in lacustrine nanoporous shale: a theoretical model and a case study. Energy Fuels, 32(12): 12247–12258

Li X, Elsworth D (2015). Geomechanics of CO_2 enhanced shale gas recovery. J Nat Gas Sci Eng, 26: 1607–1619

Li Y, Wang Y B, Wang J, Pan Z J (2020b). Variation in permeability during CO_2-CH_4 displacement in coal seams: part 1-experimental insights. Fuel, 263: 116666

Li Y, Wang Z S, Pan Z J, Niu X L, Yu Y, Meng S Z (2019a). Pore structure and its fractal dimensions of transitional shale: a cross-section from east margin of the Ordos Basin, China. Fuel, 241: 417–431

Li Y, Yang J H, Pan Z J, Meng S Z, Wang K, Niu X L (2019b). Unconventional natural gas accumulations in stacked deposits: a discussion of Upper Paleozoic coal-bearing strata in the east margin of the Ordos Basin, China. Acta Geologica Sinica (English Edition), 93(1): 111–129

Li Y, Yang J H, Pan Z J, Tong W S (2020c). Nanoscale pore structure and mechanical property analysis of coal: an insight combining AFM and SEM images. Fuel, 260: 116352

Li Z, Elsworth D (2019). Controls of CO_2–N_2 gas flood ratios on enhanced shale gas recovery and ultimate CO_2 sequestration. J Petrol Sci Eng, 179: 1037–1045

Liu J, Xie L, Elsworth D, Gan Q (2019). CO_2/CH_4 competitive adsorption in shale: implications for enhancement in gas production and reduction in carbon emissions. Environ Sci Technol, 53(15): 9328–9336

Liu J, Xie L, He B, Gan Q, Zhao P (2021a). Influence of anisotropic and heterogeneous permeability coupled with *in-situ* stress on CO_2 sequestration with simultaneous enhanced gas recovery in shale: Quantitative modeling and case study. Int J Greenh Gas Control, 104: 103208

Liu J, Xie L, He B, Zhao P, Ding H (2021b). Performance of free gases during the recovery enhancement of shale gas by CO_2 injection: a case study on the depleted Wufeng–Longmaxi shale in northeastern Sichuan Basin, China. Petrol Sci,

Liu J, Yao Y, Elsworth D, Liu D, Cai Y, Dong L (2017a). Vertical heterogeneity of the shale reservoir in the Lower Silurian Longmaxi Formation: analogy between the southeastern and northeastern Sichuan Basin, SW China. Minerals (Basel), 7(8): 151

Liu J, Yao Y, Liu D, Elsworth D (2017b). Experimental evaluation of CO_2 enhanced recovery of adsorbed-gas from shale. Int J Coal Geol, 179: 211–218

Liu J, Yao Y, Liu D, Pan Z, Cai Y (2017c). Comparison of three key marine shale reservoirs in the southeastern margin of the Sichuan Basin, SW China. Minerals (Basel), 7(10): 179

Liu J, Yao Y, Zhu Z, Cheng L, Wang G (2016). Experimental investigation of reservoir characteristics of the upper Ordovician Wufeng Formation shale in middle–upper Yangtze region, China. Energy Exploration & Exploitation, 34(4): 527–542

Liu S, Fang H, Sang S, Ashutosh T, Wu J, Zhang S, Zhang B (2020). CO_2 injectability and CH_4 recovery of the engineering test in qinshui Basin, China based on numerical simulation. Int J Greenh Gas Control, 95: 102980

Luo C J, Zhang D F, Lun Z M, Zhao C P, Wang H T, Pan Z J, Li Y H, Zhang J, Jia S Q (2019). Displacement behaviors of adsorbed coalbed methane on coals by injection of SO_2/CO_2 binary mixture. Fuel, 247: 356–367

Mazumder M, Chen L, Xu Q (2020). Integrated ejector-based flare gas recovery and on-site desalination of produced water in shale gas production. Chem Eng Technol, 43(2): 200–210

Mohagheghian E, Hassanzadeh H, Chen Z (2019). CO_2 sequestration coupled with enhanced gas recovery in shale gas reservoirs. Journal of CO_2 Utilization, 34: 646–655

Pan Y, Hui D, Luo P, Zhang Y, Sun L, Wang K (2018). Experimental investigation of the geochemical interactions between supercritical co_2 and shale: implications for co_2 storage in gas-bearing shale formations. Energy Fuels, 32(2): 1963–1978

Pan Z, Ma Y, Connell L D, Down D I, Camilleri M (2015). Measuring anisotropic permeability using a cubic shale sample in a triaxial cell. Journal of Natural Gas ence & Engineering, 26: 336–344

Shan C, Zhang T, Wei Y, Zhang Z (2017). Shale gas reservoir characteristics of Ordovician-Silurian formations in the central Yangtze area, China. Front Earth Sci, 11(1): 184–201

Su W, Li Z, Ettensohn F, Johnson M, Huff W, Wang W, Ma C, Li L, Zhang L, Zhao H (2007). Tectonic and eustatic control on the distribution of black-shale source beds in the Wufeng and Longmaxi formations (Ordovician-Silurian), South China. Front Earth Sci

China, 1(4): 470–481

Sun H, Yao J, Gao S H, Fan D Y, Wang C C, Sun Z X (2013). Numerical study of CO_2 enhanced natural gas recovery and sequestration in shale gas reservoirs. Int J Greenh Gas Control, 19: 406–419

Tao Z, Bielicki J M, Clarens A F (2014). Physicochemical factors impacting CO_2 sequestration in depleted shale formations: the case of the Utica shale. Energy Procedia, 63: 5153–5163

Vega B, Dutta A, Kovscek A R (2014). CT imaging of low-permeability, dual-porosity systems using high X-ray contrast gas. Transp Porous Media, 101(1): 81–97

Wang M, Lun Z M, Zhao C P, Wang H T, Luo C J, Fu X X, Li C, Zhang D F (2020). Influences of primary moisture on methane adsorption within Lower Silurian Longmaxi Shales in the Sichuan Basin, China. Energy Fuels, 34(9): 10810–10824

Wang T, Tian S, Li G, Sheng M, Ren W, Liu Q, Zhang S (2018). Molecular simulation of CO_2/CH_4 competitive adsorption on shale kerogen for co_2 sequestration and enhanced gas recovery. J Phys Chem C, 122(30): 17009–17018

Zhang G, Zhou W, Ji S, Liu J, Zhang J, Yang H (2015). Experimental study on CO_2 replacement method used in shale gas exploration. Journal of Chengdu University of Technology, 42(3): 366–371

Zhang H, Diao R, Mostofi M, Evans B (2020). Monte carlo simulation of the adsorption and displacement of CH_4 by CO_2 injection in shale organic carbon slit micropores for CO_2 enhanced shale gas recovery. Energy Fuels, 34(1): 150–163

Zhang K, Jiang H, Qin G (2019). Utilization of zeolite as a potential multi-functional proppant for CO_2 enhanced shale gas recovery and CO_2 sequestration: a molecular simulation study on the competitive adsorption of CH_4 and CO_2 in zeolite and organic matter. Fuel, 249 (1): 119–129

Zhang L, Lu S, Jiang S, Xiao D, Chen L, Liu Y, Zhang Y, Li B, Gong C (2018). Effect of shale lithofacies on pore structure of the Wufeng-Longmaxi Shale in southeast Chongqing, China. Energy Fuels, 32 (6): 6603–6618

Zhang P, Lu S, Li J, Xue H, Li W, Zhang P (2017). Characterization of shale pore system: a case study of Paleogene Xingouzui Formation in the Jianghan basin, China. Mar Pet Geol, 79: 321–334

Zhao P, Xie L, He B, Liu J (2020). Strategy optimization on industrial CO_2 sequestration in the depleted Wufeng-Longmaxi Formation shale in the northeastern Sichuan Basin, SW China: from the perspective of environment and energy. ACS Sustain Chem& Eng, 8 (30): 11435–11445

Zhou J, Hu N, Xian X, Zhou L, Tang J, Kang Y, Wang H (2019a). Supercritical CO_2 fracking for enhanced shale gas recovery and CO_2 sequestration: results, status and future challenges. Advances in Geo-Energy Research, 3(2): 207–224

Zhou J, Jin Z, Luo K H (2019b). Effects of Moisture contents on shale gas recovery and CO_2 sequestration. Langmuir, 35(26): 8716–8725

Zhou J, Liu M, Xian X, Jiang Y, Liu Q, Wang X (2019c). Measurements and modelling of CH_4 and CO_2 adsorption behaviors on shales: implication for CO_2 enhanced shale gas recovery. Fuel, 251: 293–306